Journal of Environmental Chemical Engineering 9 (2021) 104706

Contents lists available at ScienceDirect

Journal of Environmental Chemical Engineering

journal homepage: www.elsevier.com/locate/jece

Removal of uranium(VI) from aqueous solution by $Mg(OH)_2$-coated nanoscale zero-valent iron: Reactivity and mechanism

Chen Chen [a], Xiaowen Zhang [a,b,*], Tianjiao Jiang [a], Mi Li [a,b], Ying Peng [a,b], Xudong Liu [a], Jian Ye [a,b], Yilong Hua [a,b]

[a] School of Resource & Environment and Safety Engineering, University of South China, Hengyang, 421001, China
[b] Hengyang Key Laboratory of Soil Pollution Control and Remediation, University of South China, Hengyang 421001, China

ARTICLE INFO

Editor: G. Palmisano

Keywords:
Uranium
Nanoscale zero-valent iron
$Mg(OH)_2$coating
Suspension stability
Mobility
Layered double hydroxides

ABSTRACT

Nanoscale zero-valent iron (nZVI) is considered to be an effective material for removing U(VI), but its application in in-situ remediation is limited due to its easy oxidation and agglomeration. In order to solve this problem, nZVI@$Mg(OH)_2$ was synthesized by modified liquid phase reduction method and used to remove U(VI) from aqueous solution. The effects of pH, contact time, dosage and initial concentration on the removal of U(VI) by nZVI@$Mg(OH)_2$ were studied by batch experiments. The results showed that nZVI@$Mg(OH)_2$ presented better removal efficiency than nZVI, the removal ratio and amount reached 97.8 % and 122.3 mg/g respectively at 0.4 g/L dosage with 50 mg/L U(VI) solution. Various techniques were implemented to characterize nZVI@$Mg(OH)_2$. The results indicated that $Mg(OH)_2$ was successfully coated on the nZVI surface, thus turned rough, aggregation and oxidation of Fe° particles was minimized, then the removal performance of U(VI) increased. Mechanisms were also explored by a comparative study of the phase, morphology, and surface valence state of composite before and after reaction, indicating that nZVI@$Mg(OH)_2$ remove U(VI) mainly through reduction and adsorption. The results of column experiments and sedimentation experiments showed that the suspension stability and mobility of nZVI have been improved after coating. It can be seen that nZVI@$Mg(OH)_2$ has certain potential for in-situ remediation of U(VI).

1. Introduction

A large amount of uranium (U)-containing wastewater is discharged into nature through activities in the process of nuclear fuel production, such as uranium mining and metallurgy, purification, conversion and enrichment, they will cause internal radiation and damage the human's kidney and liver, even cause cancer after they entering the body through groundwater or other media [1]. Therefore, the treatment of uranium-containing wastewater has attracted extensive attention. Currently, a variety of methods have been used to treat uranium in groundwater, including adsorption [2,3], chemical reduction [4,5] and biological treatment, etc. [6,7]. Among them, the chemical reduction can transform the soluble and highly toxic U(VI) into the insoluble and low toxicity U(IV), which is more conducive to the precipitation and fixation of uranium in the later stage, and is considered to be the most ideal way to fix uranium for a long time. Therefore, chemical reduction is a potential method for in-situ remediation of uranium [8].

In recent years, nanoscale zero-valent iron (nZVI) has received widespread attention as a highly efficient and strong reducing agent [9–16]. Nanoscale zero-valent iron particles have the advantages of large specific surface area, multiple active sites, and strong reducibility [17], and it has been proven that nZVI can be used to remove a variety of pollutants, such as chlorinated organics, inorganic anions, heavy metals and other pollutants with high oxidation states [18–20]. For U(VI) in solution, nZVI fixes it mainly through three processes of adsorption, reduction and co-precipitation, and shows a good removal effect [21]. Ling and Zhang [22] fixed U(VI) in aqueous solution with nZVI, and the results showed that 1 g/L of nZVI could remove more than 90 % of U(VI) in only 2 min. However, due to its high reactivity and inherent magnetic interaction, nZVI is prone to agglomeration and oxidation [23], resulting in the decline of its reactivity and mobility performance, which brings challenges to in-situ remediation by nZVI.

In order to solve this problem, scholars have developed a variety of potential methods. For example, using porous carbon materials to

* Corresponding author at: School of Resource & Environment and Safety Engineering, University of South China, Hengyang, 421001, China.
E-mail address: Shawn_zhang@sina.com (X. Zhang).

https://doi.org/10.1016/j.jece.2020.104706
Received 30 August 2020; Received in revised form 13 October 2020; Accepted 28 October 2020
Available online 5 November 2020
2213-3437/© 2020 Elsevier Ltd. All rights reserved.

support nZVI and increase its adsorption capacity by increasing the specific surface area of nZVI [24,25]; improving the reactivity and stability of nZVI by sulfide modification [26–29]. In addition, the layered double hydroxides (LDH) can be constructed on the surface of nZVI to improve the oxidation and agglomeration of nVZI through electrostatic repulsion and spatial resistance [30], thus improving the reaction and migration capacity of nZVI [31–33]. Among the layered double hydroxides, $Mg(OH)_2$ has the advantages of strong stability, low cost, environmental friendliness and good adsorbability [34]. In addition, $Mg(OH)_2$ has a low solubility and is less affected by Ca^{2+}-rich groundwater when applied to in-situ remediation, which is conducive to the improvement of nZVI mobility [35]. Therefore, $Mg(OH)_2$ is considered to be a good material for coating nZVI.

In this study, we aim to synthesize an $Mg(OH)_2$ inorganic coated shell on the surface of nZVI (nZVI@$Mg(OH)_2$) to improve the reaction and migration capacity of nZVI, and to remove U(VI) from underground water of stope after in-situ leaching. The effects of pH, initial concentration of U(VI), dosage of nZVI@$Mg(OH)_2$ and contact time on the removal ability of U(VI) were studied through batch experiments. The stability and mobility performance of nZVI before and after coating were explored by settlement test and column breakthrough experiment. The nZVI@$Mg(OH)_2$ particles before and after reaction were analyzed by scanning electron microscopy (SEM), transmission electron microscopy (TEM), X-ray diffraction (XRD), X-ray photoelectron spectroscopy (XPS) and Brunauer-Emmett-Teller (BET). According to the analysis results, the process and mechanism of removing U(VI) from groundwater by nZVI@$Mg(OH)_2$ were revealed.

2. Materials and methods

2.1. Materials

Ferrous sulphate heptahdyrate ($FeSO_4{\cdot}7H_2O$, ≥99 %), sodium borohydride ($NaBH_4$, ≥99.5 %), magnesium hydroxide ($Mg(OH)_2$, ≥98 %) were purchased from Sinopharm Chemical Reagent Co., Ltd. (Shanghai, China), anhydrous ethanol (≥99.7 %) was purchased from Hunan Huihong Reagent Co., Ltd. (Hunan, China). All the chemicals were analytical grade and used without further purification. In this experiment, the solutions were all prepared with deionized water and bubbled with nitrogen for 15 min before use to remove the dissolved oxygen in the water. The U(VI) standard solution is prepared by adding HCl and H_2O_2 (30 %) to U_3O_8 (99.99 %), dissolving it in concentrated nitric acid and diluting it with deionized water.

2.2. Preparation of nZVI and nZVI@$Mg(OH)_2$

Bare nZVI was prepared by liquid phase reduction method [11], and the reaction equation is shown in Eq. (1). The whole process was carried out under the protection of nitrogen. First, 2 g $FeSO_4{\cdot}7H_2O$ was dissolved in a 100 mL solution (water: anhydrous ethanol = 3:7), stirred evenly and transferred to a 500 mL three-necked flask. Then, 100 mL 0.2 mol/L $NaBH_4$ was slowly added through peristaltic pump (BT100LC) at a speed of 5 mL/min to gradually produce black solid under the stirring of magnetic agitator (200 r/min). After adding, continue to stir 0.5 h, then washed with deoxygenated deionized water and anhydrous ethanol alternately for several times and dry in a vacuum drying oven for later use (45 °C,12 h). The prepared nZVI was used as a parallel sample to compare with nZVI@$Mg(OH)_2$.

$$Fe^{2+} + 2BH_4^- + 6H_2O = Fe^0 + 2B(OH)_3 + 7H_2\uparrow \quad (1)$$

NZVI@$Mg(OH)_2$ was prepared by sodium borohydride reduction method modified by previous [36]. The whole synthesis process was assisted by nitrogen and mechanical agitation. The specific steps are as follows: 2 g $FeSO_4{\cdot}7H_2O$ was dissolved in a 50 mL deoxygenated deionized water, stirred evenly and transferred to a 500 mL three-necked flask. Then, 0.3 g $Mg(OH)_2$ was dissolved in 50 mL anhydrous ethanol and sonicate for 10 min and transferred to the flask. After the solution was evenly mixed, 100 mL of 0.2 mol/L $NaBH_4$ was added at the rate of 5 mL/min, and continued to stirred another 1 h after adding. In this process, $Mg(OH)_2$ gradually accumulated on the outer layer of nZVI to form inorganic coating layer. The products were washed alternately with deoxygenated deionized water and anhydrous ethanol to remove impurities, and magnets were used for separation during the washing process. After washing, the samples were dried in a vacuum drying oven for later use (45 °C, 12 h).

2.3. Determination of iron content

The iron content is measured by the stannous chloride reduction titration method (GB/T 6730.70-2013) [37]. Specific steps are as follows: A certain amount of nZVI@$Mg(OH)_2$ particles was added to 150 mL conical flask, followed by HCl and HF for digestion on the heating plate (250 °C). After digestion, a few drops of $SnCl_2$ was added until the solution becomes colorless and added two more drops. Then, added 10 mL $HgCl_2$ and deionized water to about 100 mL. Finally, 20 mL of sulfur-phosphorus mixed acid (15 %H_2SO_4-15 %H_3PO_4-70 %H_2O) and drops of sodium diphenylamine sulfonate indicator were added and titrated with potassium dichromate solution until the solution turned purple. The calculation method is shown in Eq. (2).

$$M_{Fe} = 0.002 \times V \quad (2)$$

where, M_{Fe} is the content of Fe in the sample to be tested (g), V is the amount of K_2CrO_4 consumed during titration (mL).

2.4. Characterization

Scanning electron microscopy (SEM, SIGMA300, Germany) and transmission electron microscopy (TEM, JEM2010, Japan) were used to analyze the morphology and microstructure of nZVI and nZVI@$Mg(OH)_2$. At the same time, X-ray energy dispersive spectrometer (EDS, QUANTA400FEG, USA) was used to analyze the elemental composition of nZVI prior to and after reaction. Crystal characteristics of the sample were studied at room temperature using an X-ray diffraction (XRD, UltimaIV, Japan). It was equipped with XRD-DSC diffraction device, with a step length of 0.02°, a scanning speed of 10°/min, and a diffraction angle (2θ) of 10-80°. The surface composition was measured with X-ray photoelectron spectroscopy (XPS, ESCALAB250xi, USA), and the pore size and specific surface area of nZVI before and after coating were measured by Brunauer-Emmett-Teller method (BET, ASAP2460, USA).

2.5. Batch experiments

The entire batch experiment was always carried out in a shaking table reactor at 25 °C, and the content of U in the solution was measured by Arsenazo(III) method [38]. Each experiment was conducted in parallel. First, the standard curve of U(VI) was drawn to calculated the relationship between absorbance and concentration, which can be used to calculated the subsequent concentration of U(VI). Then, 1 g/L uranium standard solution was diluted to 5−50 mg/L with deionized water, and 0.1 mol/L NaOH and HCl were used to adjust the pH of the solution (pH 3–8) for the batch experiment. Briefly, a certain amount (0.1–2.0 g/L) of nZVI and nZVI@$Mg(OH)_2$ particles were added to a 150 mL conical flask filled with 50 mL U(VI) solution, injected nitrogen and sealed with rubber stopper. After shaking a certain time (10−60 min), the suspensions were filtered and added the hydrochloric acid, arsenazo (III), buffer solution and masking agent in sequence. Finally, absorbance was measured using a visible spectrophotometer (UV-3200) at 652 nm and U(VI) concentration was calculated according to the standard curve. Removal ratio of U(VI) (R, %) and removal capacity (Q, mg/g) were

calculated by Eq. (3) and Eq. (4), respectively.

$$R = \frac{C_0 - C_1}{C_0} \times 100\% \quad (3)$$

$$Q = \frac{(C_0 - C_1)V}{m} \quad (4)$$

where, C_0 and C_1 are the uranium(VI) concentration measured before and after reaction (mg L^{-1}), respectively; V is the volume of solution (L), and m is the weight of the material (g).

2.6. Sedimentation experiments

The static sedimentation experiment was carried out in order to study the suspension stability of nZVI@$Mg(OH)_2$ particles in deionized water [39]. First, 50 mL 0.2 g/L nZVI and nZVI@$Mg(OH)_2$ suspension were prepared and dispersed fully by sonicated for 10 min. Then, placed in two 50 mL centrifuge tubes respectively for a vertical static state, and photographs were taken to observe and compare their settlement states within a certain period time.

2.7. Column breakthrough experiments

The mobility of material is directly related to its application in in-situ remediation, as it determines whether the material can reach the contaminated underground area and restore the target pollutant [40]. The column breakthrough experiments were carried out to study the mobility performance of nZVI and nZVI@$Mg(OH)_2$ particles. A 1.1-cm-diam glass column was filled with quartz sand (D = 850 μm) to a height of 20 cm. The pore volume (PV) of the column was calculated as 3.5 mL and the porosity was 0.18. The filter material was soaked in 0.1 M HCl for 24 h before use to remove impurities, and washed with deionized water until neutrality, then dried for use. The nylon mesh and glass beads were placed underneath the filter before filling to prevent quartz sand from draining.

The experimental steps are as follows: First, 10 PV deionized water was added to the glass column to keep it saturated, and 10 mL 2.5 g/L nZVI or nZVI@$Mg(OH)_2$ suspensions were injected from the top (10 mL/min), respectively. Then, the sand column was washed successively with 2−14 PV deionization water (2.2 mL/min), and an erlenmeyer flask was connected below the glass column. Suspension in the erlenmeyer flask were dissolved with hydrochloric acid after no solution was discharged, and the total iron content was measured by the stannous chloride reduction titration method (GB/T 6730.70-2013). Finally, the breakthrough curve was obtained with the pore volume (PV) as the abscissa and M/M_0 (iron mobility rate) as the ordinate.

3. Results and discussion

3.1. Characterization of nZVI and nZVI@$Mg(OH)_2$

The surface morphology of nZVI and nZVI@$Mg(OH)_2$ was characterized by SEM (Fig. 1**(a, b)**). It can be seen from Fig. 1**(a)** that the nZVI synthesized by borohydride reduction is spherical or ellipsoidal, with

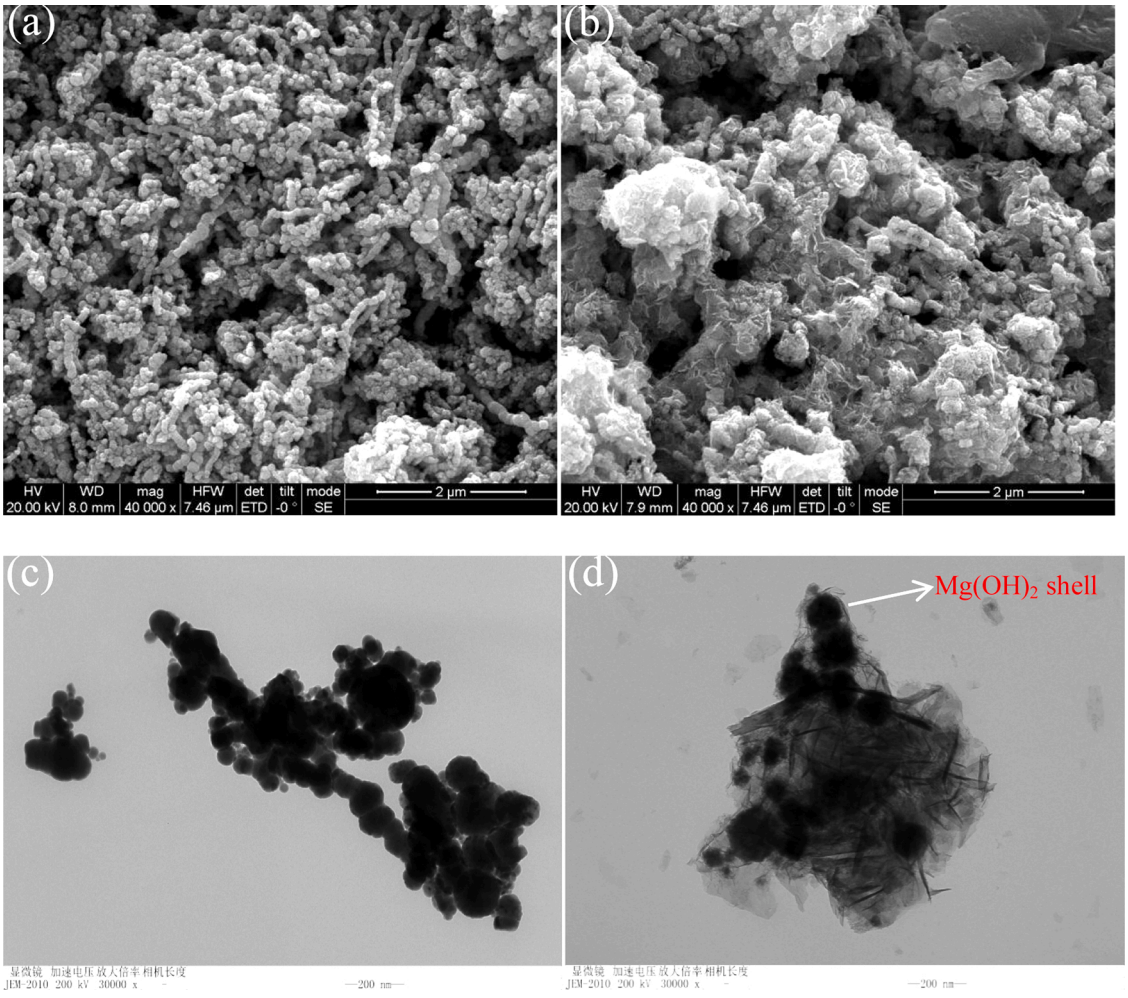


Fig. 1. SEM images of (a) nZVI, (b) nZVI@$Mg(OH)_2$ and TEM images of (c) nZVI, (d) nZVI@$Mg(OH)_2$.

uniform distribution, smooth surface and mostly chain distribution. However, nZVI@Mg(OH)$_2$ (Fig. 1**(b)**) is not uniformly distributed, and the surface becomes rough due to the formation of sediments, which is similar to the conclusions of other scholar [30]. EDS images of nZVI and nZVI@Mg(OH)$_2$ are shown in Fig. 2. It can be seen from Fig. 2**(a)** that oxygen element exists in the synthesized nZVI particles, indicating that the oxidation of nZVI inevitably occurs. Fig. 2**(b)** shows that Mg element appears in the coated nZVI sample, which proves that the surface of nZVI was successfully coated with Mg(OH)$_2$. In addition, the proportion of Fe has also increased from 51.3 % of nZVI to 64.2 % of nZVI@Mg(OH)$_2$, which can be explained by that the Mg(OH)$_2$ coating layer reduces the oxidation of nZVI.

TEM images (Fig. 1**(c, d)**) show that the particle size of nZVI was relatively uniform, with the diameter of a single particle about 100 nm, and the particles agglomerate and present a chain shape due to the inherent magnetic attraction and van der waals force of nZVI (Fig. 1**(c)**). It can be seen from Fig. 1**(d)** that the surface of nZVI is covered by a layer of coating, and the coated nZVI has better dispersibility without serious aggregation, which is similar to Zhang et al. [41] reported. That suggested the Mg(OH)$_2$ shell on the surface reduces the magnetic attraction between nZVI particles through spatial resistance and electrostatic repulsion [42].

It can be seen from **Fig. S1** that nZVI has an obvious XRD diffraction peak at 2θ = 44.7°, corresponding to the plane of (110) α-Fe (JCPDS#99-0064). In addition, no other obvious diffraction peaks are found, indicating that the synthesized nZVI is of high purity. Except for the same diffraction peak of α-Fe, new peaks appear at 2θ = 18.6°, 38.1°, 50.9°, and 58.7° after coating, corresponding to planes of (001), (011), (012), (110) with Mg(OH)$_2$ (JCPDS#78-0316), see in **Fig. S1.** These proved again that Mg(OH)$_2$ was successfully coated on the surface of nZVI. Different from other scholars, the diffraction peak of α-Fe in nZVI@Mg(OH)$_2$ was not weakened after coating, indicating that the formation of Mg(OH)$_2$ inorganic shell did not affect the crystallization state of Fe.

The specific surface area of nZVI and nZVI@Mg(OH)$_2$ were measured with the Brunauer-Emmett-Teller method, which were 15.0 m^2/g and 20.4 m^2/g, respectively. It can be seen that specific surface area of nZVI has been improved after coating. In addition, the average pore size and total pore volume have also increased from 10.6 nm and 0.04 cm^3/g to 16.8 nm and 0.09 cm^3/g, respectively. That suggests the Mg(OH)$_2$ shell reduces the magnetic attraction between particles through shielding and increases the distance between particles, which is consistent with the results observed by TEM image (Fig. 1**(c, d)**). The nZVI particles with increased surface area and pore size will gain more active sites, thus enhancing the removal of U(VI) by nZVI [43].

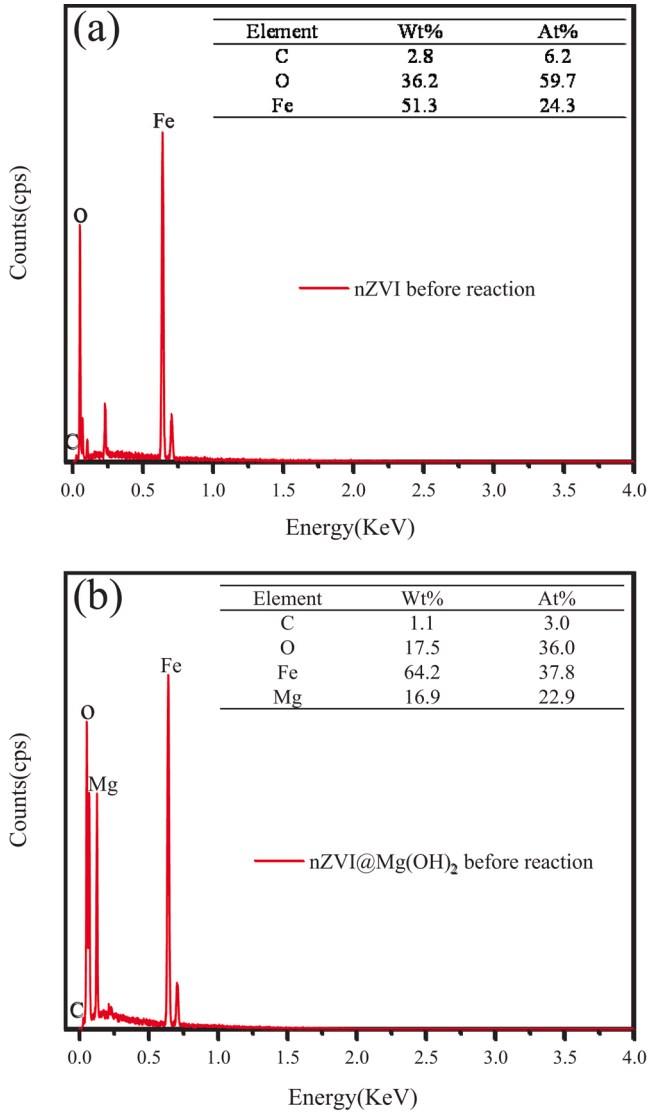


Fig. 2. EDS images of (a) nZVI and (b) nZVI@Mg(OH)$_2$.

3.2. Removal of U(VI) by nZVI@Mg(OH)$_2$

3.2.1. Effect of initial pH

The pH of solution is an important factor that affects the removal of heavy metal ions, because the existence of heavy metals, surface charges and binding sites of materials at different pH values are different [44]. Therefore, we studied the removal of U(VI) by nZVI@Mg(OH)$_2$ at pH 3–8. It can be seen in Fig. 3(a) that the removal ratio of U(VI) by nZVI@Mg(OH)$_2$ reaches the maximum value at pH = 3, both the removal ratio and removal amount show a downward trend with the increase of pH, which is similar to the conclusion of Wu et al. [45]. This can be explained by that it is more favorable to Mg(OH)$_2$ shell on the nZVI surface dissolve under acidic conditions, and the occurrence of the dissolution reaction is conducive to the activation of the nZVI reaction performance. For nZVI, the removal ratio of U(VI) is low at pH = 3, and both the removal ratio and removal amount are greatly improved with the increase of pH from 3 to 5. These can be explained by two reasons: On the one hand, H^+ reacts with Fe^0 to form Fe^{2+} under strong acid conditions, and hydroxides of Fe will be formed on the surface of nZVI particles with the increase of Fe^{2+}, which will hinder the removal of U (VI). On the other hand, H^+ in the solution will compete with UO_2^{2+} for the active adsorption site of nZVI, thus generating electrostatic repulsion, which will also hinder the reaction between UO_2^{2+} and nZVI particles, and ultimately lead to a decrease in the removal ratio and removal amount of U(VI) [46]. So, nZVI@Mg(OH)$_2$ has stronger acid resistance than nZVI.

When the pH is close to neutral or weak alkaline (pH 6–8), the removal ratio and removal amount of U(VI) by nZVI and nZVI@Mg (OH)$_2$ both show a downward trend, which is due to the decrease of H^+, leads to the decrease of shell dissolution and the reactive active site, moreover, UO_2^{2+} will be hydrolyzed to produce $[(UO_2)_3(OH)_5]^+$, $[(UO_2)_2(OH)_2]^{2+}$, $[UO_2(OH)]^+$ and other complexes [47], these complexes will inhibit the adsorption and reduction of U(VI) by nZVI@Mg (OH)$_2$, thereby reduce the removal rate and removal amount of U(VI). Considering that the optimum pH for removing U(VI) with nZVI and nZVI@Mg(OH)$_2$ is different, the subsequent batch experiments with nZVI and nZVI@Mg(OH)$_2$ were carried out under the conditions of pH = 5 and pH = 3, respectively.

3.2.2. Effect of contact time

The effect of contact time on the removal of U(VI) by nZVI@Mg (OH)$_2$ was studied in the range of 10−60 min. It can be seen from Fig. 3 **(b)** that the removal reaction of U(VI) by nZVI and nZVI@Mg(OH)$_2$

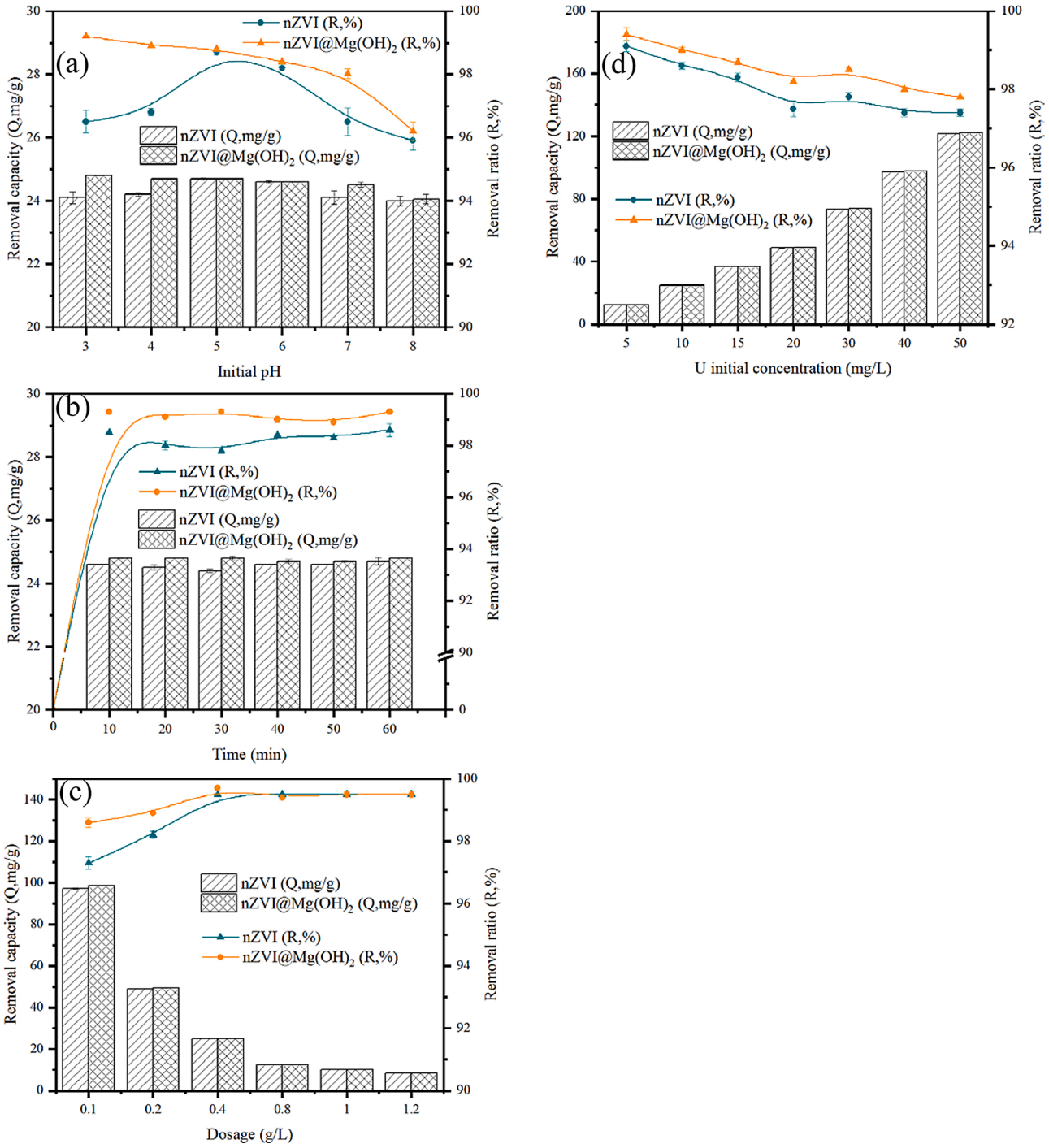


Fig. 3. Effects of different factors on U(VI) removal. (a): initial pH, C_0 = 10 mg/L; dosage = 0.4 g/L; T = 25 °C; contact time = 60 min. (b): contact time, C_0 = 10 mg/L; dosage = 0.4 g/L; T = 25 °C; initial pH(nZVI = 5.0, nZVI@Mg(OH)$_2$ = 3.0). (c): dosage, C_0 = 10 mg/L; contact time = 60 min; T = 25 °C; initial pH(nZVI = 5.0, nZVI@Mg(OH)$_2$ = 3.0). (d): U(VI) initial concentration, dosage = 0.4 g/L; contact time = 60 min; T = 25 °C; initial pH(nZVI = 5.0, nZVI@Mg(OH)$_2$ = 3.0).

reached equilibrium within a short period of 10 min. In the initial stage (0−10 min), the concentration of U(VI) was relatively high, and the active groups on the surface of nZVI@Mg(OH)$_2$ can fully contact with U (VI). However, in the later stage (10−60 min), precipitates of Fe and U were formed on the surface of nZVI@Mg(OH)$_2$ with the decrease of nZVI@Mg(OH)$_2$ active sites and U(VI), which hindered the adsorption and reduction of nZVI@Mg(OH)$_2$ particles on U(VI), thus affected the further growth of removal rate and removal amount. Taking into account that there may be uneven contact between nZVI@Mg(OH)$_2$ particles and U(VI), the contact time was controlled to 60 min in subsequent experiments, which can better ensure the accuracy of subsequent experiments.

3.2.3. *Effect of nZVI@Mg(OH)$_2$ dosage*

The nZVI@Mg(OH)$_2$ dosage is an important parameter for the influence on reaction equilibrium. Moreover, in order to achieve economy in in-situ remediation, comprehensive consideration should be given to it [45]. Under certain other conditions, the effect of nZVI@Mg(OH)$_2$ dosage on U(VI) removal was studied (Fig. 3**(c)**). It is seen that the removal rate showed an upward trend with the increase of dosage, while

the removal amount showed a downward trend. That can be explained by the total surface area and active sites increase by nZVI@$Mg(OH)_2$ dosage, which is more conducive to the adsorption and reduction of U (VI) [48]. However, a certain amount of U(VI) solution requires a limited number of active sites, and with the increase of the added amount, the remaining active sites will increase, leading to a decrease in the removal amount of coated material per unit weight.

In addition, it was easy to find in Fig. 3**(c)** that the removal ratio of nZVI@$Mg(OH)_2$ was higher than nZVI when the dosage was less than 0.4 g/L, which indicated that nZVI@$Mg(OH)_2$ has more potential in U (VI) removal. Considering the high efficiency and economy required for in-situ remediation, a dosage of 0.4 g/L is appropriate.

3.2.4. *Effect of U(VI) initial concentration*

The effect of different U(VI) initial concentrations was studied in the range of 5−50 mg/L, and the results are shown in Fig. 3**(d)**. It can be seen that the removal ratio gradually decreased by the increase of U(VI) initial concentration, and the removal ratio of U(VI) with nZVI@Mg$(OH)_2$ decreased from 99.4 % at 5 mg/L to 97.8 % at 50 mg/L, respectively. This can be interpreted as high-concentration U(VI) solutions require more active sites, and a certain amount of nZVI@$Mg(OH)_2$ had limited removal capacity [49], which leaded to a decrease in removal ratio. On the contrary, the removal amount was significantly increased with the increase of the initial concentration, because that high concentration of U(VI) made more full use of the active site on the surface of nZVI@$Mg(OH)_2$, and the removal amount of U(VI) was increased by improving the utilization rate of the active site.

In addition, nZVI@$Mg(OH)_2$ did not significantly increase the removal amount of U(VI) under the same added material weight compared with nZVI (Fig. 3**(d)**), but the coating of $Mg(OH)_2$ greatly improved the availability of iron with about 33.7 %, which was attributed to the fact that $Mg(OH)_2$ coating reduces the agglomeration and oxidation of nZVI and improves the dispersion and stability of nZVI.

3.3. *Stability and mobility of nZVI@Mg(OH)$_2$*

In order to compare the mobility performance of nZVI and nZVI@Mg$(OH)_2$ in porous media, a quartz sand column breakthrough experiment was carried out (Fig. 4). It can be seen that the mobility of nZVI@Mg$(OH)_2$ is significantly better than nZVI. The normalized concentration (M/M_0) at the effluent end of the columns tends to rise gradually from 4.9 % of 2 PV to 16.0 % of 14 PV, an increase of 226 % for nZVI, rise from

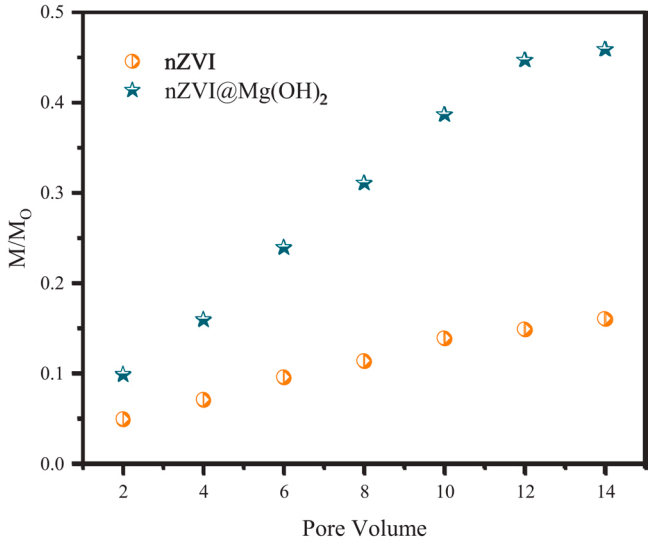


Fig. 4. Breakthrough curves of nZVI and nZVI @$Mg(OH)_2$ particles in sand volumns.

9.9 % to 45.9 %, an increase of 365 % for nZVI@$Mg(OH)_2$ correspondingly. Strong magnetism of uncoated nZVI and the agglomeration of particles attracted to each other to make the diameter and mass increased, which is easy to be trapped by quartz sand and caused gravity settlement, and, weaken its migration performance. For nZVI@Mg$(OH)_2$, it achieves better mobility performance because the steric hindrance of $Mg(OH)_2$ coating layer reduces the agglomeration of nZVI.

The static sedimentation experiment was carried out with nZVI and nZVI@$Mg(OH)_2$, **Fig. S2** are the representative pictures. It can be seen that both of them were uniformly dispersed without significant sedimentation at 1 min, nZVI almost completely settled at the bottom of the centrifuge tube at about 180 min, while nZVI@$Mg(OH)_2$ only slightly stratified, and nZVI@$Mg(OH)_2$ finally settled to the bottom in 360 min. The results show that coating of nZVI can improve its mobility performance, the dispersion and suspension ability, which are essential for the application of nZVI to in-situ remediation.

3.4. *Mechanisms of U(VI) removal by nZVI@Mg(OH)$_2$*

To better understand the removal mechanism of U(VI) by nZVI@Mg$(OH)_2$, a variety of characterization analysis was carried out on the samples before and after reaction between nZVI@$Mg(OH)_2$ and U(VI). The results are shown in Figs. 5–8. As can be seen from SEM image (Fig. 5), the nZVI@$Mg(OH)_2$ particles are spherical, chain-like and smooth before reaction (Fig. 5**(a)**). After reaction (Fig. 5**(b)**), the surface became rough and irregular in shape, which was attributed to the co-precipitation of the corrosion products of iron, the reduction products of U and the oxides of U formed on the surface of nZVI@$Mg(OH)_2$ particles [1]. EDS analysis was employed to investigate the surface state of Fe, U, C, O, and Mg with the products before and after reaction. Fig. 6 presents a detailed EDS survey, U peak appeared to the EDS image of nZVI@$Mg(OH)_2$ after reaction, indicating the existence of U in nZVI@$Mg(OH)_2$, the weight percentage and atomic percentage of U on them were 13.2 % and 1.5 % respectively.

Fig. 7 illustrates the XRD pattern of the solid sample before and after reaction. It can be seen that new diffraction peaks appear at $2\theta = 14.1°$, 27.0°, 36.3°, 46.9° after reaction, which correspond to the crystal planes (200), (210), (301), (020) of FeOOH (JCPDS#44-1415), and the diffraction peak of Fe° was weakened after reaction, indicating that Fe° was consumed during the reaction with U(VI) and other forms of iron products were generated. Also, the intensity of $Mg(OH)_2$ diffraction peak decreases slightly after reaction, and no other crystal formation of magnesium appears, all these seem to indicate that $Mg(OH)_2$ mainly plays adsorption in the reaction course.

In addition, the nZVI@$Mg(OH)_2$ samples before and after reaction were analyzed by XPS to determine their surface chemical composition. The XPS spectra of total scans, U 4f, Fe 2p and O 1s are shown in Fig. 8. As can be seen from Fig. 8**(a)**, the U 4f peak appeared after nZVI@Mg$(OH)_2$ reaction with U(VI), which indicates that U(VI) was fixed on the surface of nZVI@$Mg(OH)_2$. The U 4f spectrum (Fig. 8**(b)**) shows the photoelectron peaks at binding energies of 392.9 eV and 382.1 eV corresponding to the U $4f_{5/2}$ and U $4f_{7/2}$, respectively [50,51]. Meanwhile, the peak at binding energy of 380.6 eV belongs to UO_2 [52], which confirms the presence of redox reaction, with part of U(VI) converted to U(IV). The detailed XPS spectra of Fe 2p are shown in Fig. 8**(c, d)**. The peaks at 725.1 eV and 710.7 eV correspond to the photoelectron peaks of Fe $2p_{1/2}$ and Fe $2p_{3/2}$, respectively [36], which due to the intrinsic oxide film of Fe or oxidation during storage. The photoelectron peak of Fe° showed at the binding energy of 706.7 eV before reaction [30], and it was significantly weakened after exposure to U(VI) solution, which resulted from the oxidation of $Fe^0$to Fe(II) or Fe(III) during the reaction.

The XPS spectra of O 1s are shown in Fig. 8**(e, f)**, the binding energies of 532.6 eV, 531.4 eV, and 531.0 eV correspond to H_2O, O^{2-} and OH-, respectively [46,53,54]. After reaction, the peaks of H_2O, O^{2-}, and OH^- deviated by 0.2, 1.8, and 0.07 eV, respectively, indicating that all three were involved in the reaction. The peaks of H_2O and O^{2-} show an

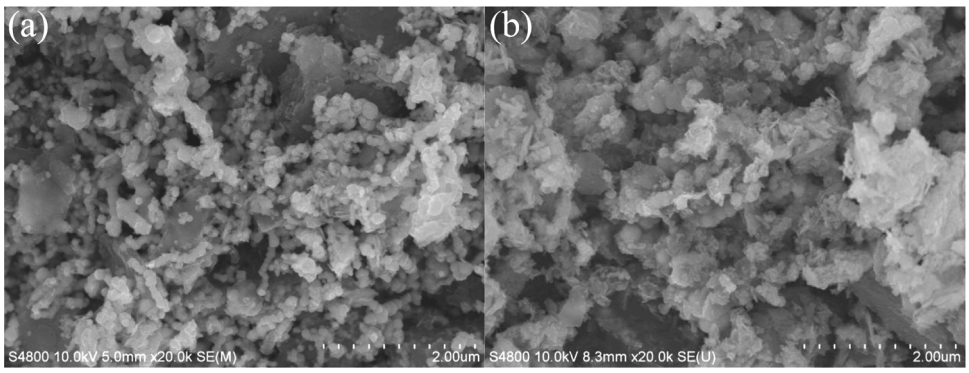


Fig. 5. SEM images of nZVI@$Mg(OH)_2$ (a) before and (b) after reaction with U(VI) (initial pH = 3; contact time = 60 min; dosage = 0.4 g/L; C_0 = 50 mg/L).

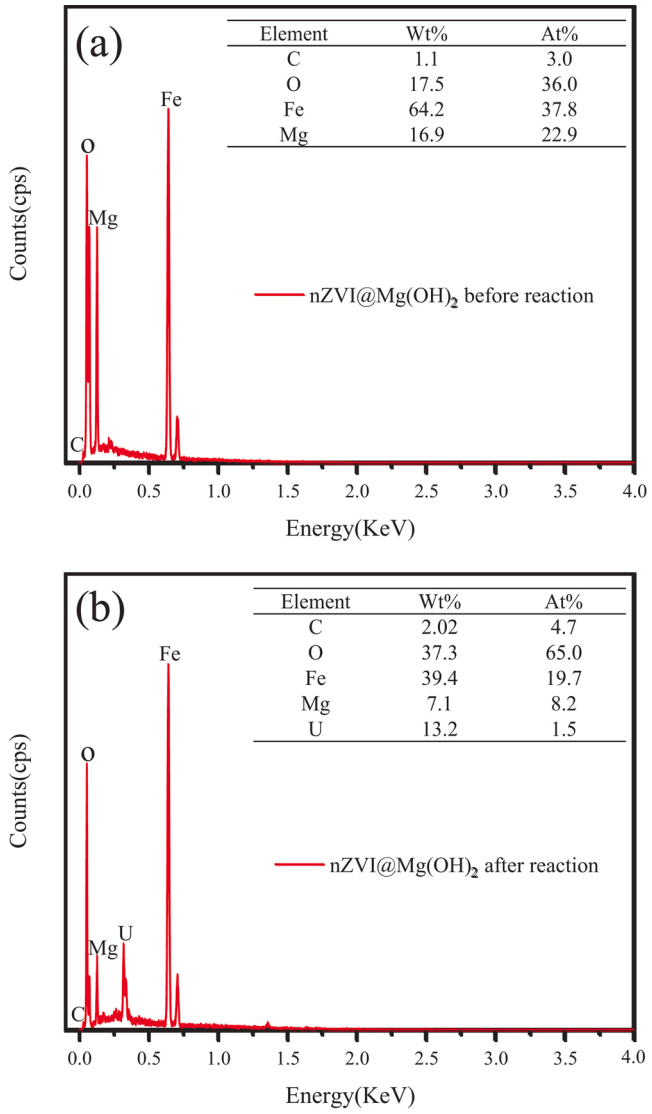


Fig. 6. EDS images of nZVI@$Mg(OH)_2$ (a) before and (b) after reaction with U (VI) (initial pH = 3; contact time = 60 min; dosage = 0.4 g/L; C_0 = 50 mg/L).

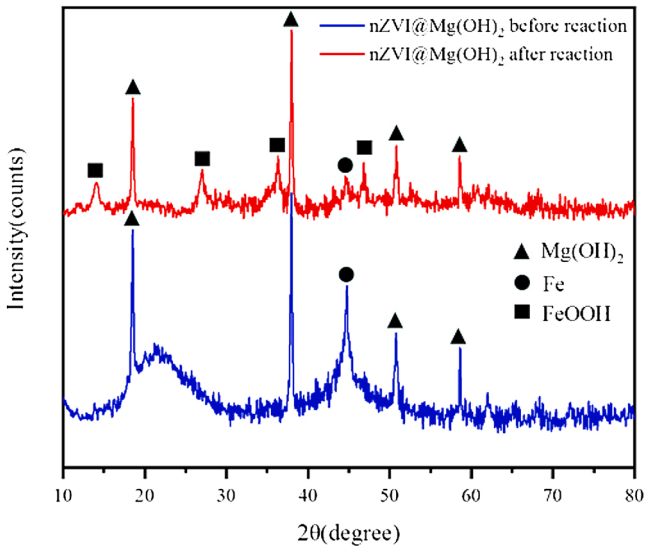


Fig. 7. XRD images of nZVI@$Mg(OH)_2$ before and after reaction with U(VI) (initial pH = 3; contact time = 60 min; dosage = 0.4 g/L; C_0 = 50 mg/L).

increasing trend, while the OH^- peaks is weakened, which due to the reduction of UO_2^{2+} to UO_2 and the formation of H_2O between OH^- and H^+, and is consistent with the conclusion drawn in Fig. 8**(b)** and Eq. (5).

In summary, the removal of U(VI) by nZVI@$Mg(OH)_2$ includes three processes: adsorption, reduction and co-precipitation [21], and the reaction equations are as follows Eqs. (5–8). First, nZVI@$Mg(OH)_2$ adsorbed U(VI) on the surface due to its large specific surface area and active adsorption sites. Then, U(VI) was reduced to U(IV) by redox, while Fe^0 was oxidized to Fe^{3+} and further produced FeOOH. Finally, Fe oxide was deposited on the surface of nZVI@$Mg(OH)_2$ together with UO_2. The $Mg(OH)_2$ coating layer on the surface of nZVI not only increases the adsorption of U(VI), but also reduces the agglomeration and oxidation of nZVI, and improves the stability and mobility of nZVI, thereby enhancing the removal of U(VI).

$$Fe^0 + 1.5UO_2^{2+} + 6H^+ = Fe^{3+} + 1.5U^{4+} + 3H_2O\uparrow \quad (5)$$

$$U^{4+} + 2H_2O \rightarrow UO_2 + 4H^+ \quad (6)$$

$$Fe^{3+} + 3OH^- = Fe(OH)_3 \quad (7)$$

$$Fe(OH)_3 + 3H^+ = FeOOH + H_2O \quad (8)$$

4. Conclusion

In this study, nZVI@$Mg(OH)_2$ was successfully synthesized and used to remove U(VI) from aqueous solution. The results of SEM, TEM and XRD analysis showed that the exist of $Mg(OH)_2$ coating could reduce the oxidation and agglomeration of nZVI particles and improve the specific surface area of nZVI. The results of sedimentation experiments and column breakthrough experiments indicated that $Mg(OH)_2$ coating can

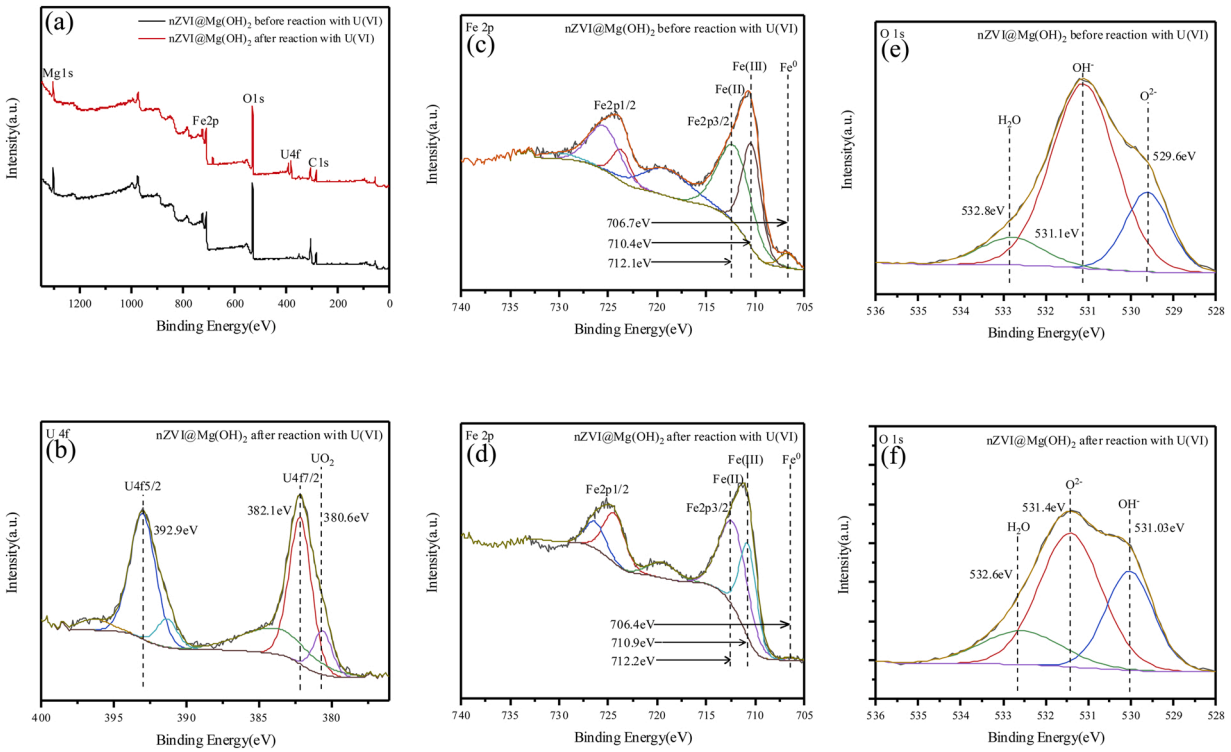


Fig. 8. XPS images of nZVI@$Mg(OH)_2$ before and after reaction with U(VI) (initial pH = 3; contact time = 60 min; dosage = 0.4 g/L; C_0 = 50 mg/L).

improve the suspension stability and mobility of nZVI particles. The results of batch experiments showed that the removal ability of nZVI@$Mg(OH)_2$ on U(VI) was improved compared with nZVI. Under the conditions of 0.4 g/L dosage and 50 mg/L initial concentration of U(VI), the removal ratio and amount reached 97.8 % and 122.3 mg/g, respectively. In addition, the removal rate of U(VI) by nZVI@$Mg(OH)_2$ increased with the increase of contact time and dosage, and decreased with the increase of pH and U(VI) initial concentration. According to the results of XPS, EDS, etc., the mechanism of uranium immobilization was analyzed, and it is shown that the interaction between nZVI@$Mg(OH)_2$ and U(VI) includes three processes of adsorption, reduction and co-precipitation. Based on the results of this study, we believe that nZVI@$Mg(OH)_2$ has certain potential for in-situ remediation of U(VI).

CRediT authorship contribution statement

Chen Chen: Writing - original draft, Writing - review & editing, Data curation, Visualization, Validation. **Xiaowen Zhang:** Writing - original draft, Writing - review & editing, Funding acquisition, Validation. **Tianjiao Jiang:** Supervision, Resources. **Mi Li:** Supervision, Resources. **Ying Peng:** Data curation. **Xudong Liu:** Data curation. **Jian Ye:** Writing - review & editing. **Yilong Hua:** Writing - review & editing.

Declaration of Competing Interest

The authors declare that they have no known competing financial interests or personal relationships that could have appeared to influence the work reported in this paper.

Acknowledgements

This study was supported by the Hunan Provincial Department of Education Scientific Research Project(Grant No. 19A417), the National Natural Science Foundation of China (Grant No. 51874180, No. 51704169), and the Science and Technology Planning Project of Hunan Province(Grant No. 2019RS2042).

Appendix A. Supplementary data

Supplementary material related to this article can be found, in the online version, at doi:https://doi.org/10.1016/j.jece.2020.104706.

References

[1] Z.J. Li, L. Wang, L.Y. Yuan, C.L. Xiao, L. Mei, L.R. Zheng, J. Zhang, J.H. Yang, Y. L. Zhao, Z.T. Zhu, Z.F. Chai, W.Q. Shi, Efficient removal of uranium from aqueous solution by zero-valent iron nanoparticle and its graphene composite, J. Hazard. Mater. 290 (2015) 26–33, https://doi.org/10.1016/j.jhazmat.2015.02.028.
[2] X.Y. Jiang, H.Q. Wang, E. Hu, Z.W. Lei, B.L. Fan, Q.L. Wang, Efficient adsorption of uranium from aqueous solutions by microalgae based aerogel, Microporous Mesoporous Mater. 305 (2020) 110383, https://doi.org/10.1016/j.micromeso.2020.110383.
[3] Y.X. Qian, Y.H. Yuan, H.L. Wang, H. Liu, J.X. Zhang, S. Shi, Z.H. Guo, N. Wang, Highly efficient uranium adsorption by salicylaldoxime/polydopamine graphene oxide nanocomposites, J. Mater. Chem. A 6 (2018) 24676–24685, https://doi.org/10.1039/C8TA09486A.
[4] J. Lin, Z.H. Yue, M.A. Silver, M.Y. Qie, X.M. Wang, W. Liu, X. Lin, H.L. Bao, L. J. Zhang, S. Wang, J.Q. Wang, In situ reduction from uranyl ion into a tetravalent uranium trimer and hexamer featuring ion-exchange properties and the alexandrite effect, Inorg. Chem. 57 (2018) 6753–6761, https://doi.org/10.1021/acs.inorgchem.8b01098.
[5] S.D. Herrmann, P.K. Tripathy, S.M. Frank, J.A. King, Comparative study of monolithic platinum and iridium as oxygen-evolving anodes during the electrolytic reduction of uranium oxide in a molten LiCl–Li_2O electrolyte, J. Appl. Electrochem. 49 (2019) 379–388, https://doi.org/10.1007/s10800-019-01287-1.
[6] A. Boghi, T. Roose, G.J.D. Kirk, A model of uranium uptake by plant roots allowing for root-induced changes in the soil, Environ. Sci. Technol. 52 (2018) 3536–3545, https://doi.org/10.1021/acs.est.7b06136.
[7] E. Marsili, H. Beyenal, L. Di Palma, C. Merli, A. Dohnalkova, J.E. Amonette, Z. Lewandowski, Uranium immobilization by sulfate-reducing biofilms grown on hematite, dolomite, and calcite, Environ. Sci. Technol. 41 (2007) 8349–8354, https://doi.org/10.1021/es071335k.
[8] B.W. Hu, F. Ye, X.M. Ren, D.L. Zhao, G.D. Sheng, H. Li, J.Y. Ma, X.K. Wang, Y. Y. Huang, X-ray absorption fine structure study of enhanced sequestration of U(VI) and Se(IV) by montmorillonite decorated with zero-valent iron nanoparticles, Environ. Sci. Nano. 3 (2016) 1460–1472, https://doi.org/10.1039/c6en00421k.
[9] D. Lv, X.X. Zhou, J.S. Zhou, Y.L. Liu, Y.Z. Li, K.L. Yang, Z. Lou, S.A. Baig, D.L. Wu, X.H. Xu, Design and characterization of sulfide-modified nanoscale zerovalent iron for cadmium(II) removal from aqueous solutions, Appl. Surf. Sci. 442 (2018) 114–123, https://doi.org/10.1016/j.apsusc.2018.02.085.
[10] Y.K. Xie, H.R. Dong, G.M. Zeng, L.H. Zhang, Y.J. Cheng, K.J. Hou, Z. Jiang, C. Zhang, J.M. Deng, The comparison of Se(IV) and Se(VI) sequestration by

nanoscale zero-valent iron in aqueous solutions: The roles of solution chemistry, J. Hazard. Mater. 338 (2017) 306–312, https://doi.org/10.1016/j.jhazmat.2017.05.053.
[11] D.L. Huang, W.J. Xue, G.M. Zeng, J. Wan, G.M. Chen, C. Huang, C. Zhang, M. Cheng, P. Xu, Immobilization of Cd in river sediments by sodium alginate modified nanoscale zero-valent iron: Impact on enzyme activities and microbial community diversity, Water Res. 106 (2016) 15–25, https://doi.org/10.1016/j.watres.2016.09.050.
[12] M. Gil-Díaz, L.F. López, J. Alonso, M.C. Lobo, Comparison of nanoscale zero-valent iron, compost, and phosphate for Pb immobilization in an acidic soil, Water. Air. Soil Pollut. 229 (2018) 1–11, https://doi.org/10.1007/s11270-018-3972-1.
[13] Y. Dai, Y.C. Hu, B.J. Jiang, J.L. Zou, G.H. Tian, H.G. Fu, Carbothermal synthesis of ordered mesoporous carbon-supported nano zero-valent iron with enhanced stability and activity for hexavalent chromium reduction, J. Hazard. Mater. 309 (2016) 249–258, https://doi.org/10.1016/j.jhazmat.2015.04.013.
[14] H.W. Wu, Q.Y. Feng, H. Yang, P. Lu, B. Gao, A. Alansari, Enhanced phenanthrene removal in aqueous solution using modified biochar supported nano zero-valent iron, Environ. Technol. (United Kingdom). 40 (2019) 3114–3123, https://doi.org/10.1080/09593330.2018.1549104.
[15] A. Toli, K. Chalastara, C. Mystrioti, A. Xenidis, N. Papassiopi, Incorporation of zero valent iron nanoparticles in the matrix of cationic resin beads for the remediation of Cr(VI) contaminated waters, Environ. Pollut. 214 (2016) 419–429, https://doi.org/10.1016/j.envpol.2016.04.034.
[16] P.D. Mines, B. Uthuppu, D. Thirion, M.H. Jakobsen, C.T. Yavuz, H.R. Andersen, Y. Hwang, Granular activated carbon with grafted nanoporous polymer enhances nanoscale zero-valent iron impregnation and water contaminant removal, Chem. Eng. J. 339 (2018) 22–31, https://doi.org/10.1016/j.cej.2018.01.102.
[17] M. Wang, W. Cheng, T. Wan, B.W. Hu, Y.L. Zhu, X.F. Song, Y.B. Sun, Mechanistic investigation of U(VI) sequestration by zero-valent iron/activated carbon composites, Chem. Eng. J. 362 (2019) 99–106, https://doi.org/10.1016/j.cej.2018.12.138.
[18] Y.Q. Liu, S.A. Majetich, R.D. Tilton, D.S. Sholl, G.V. Lowry, TCE dechlorination rates, pathways, and efficiency of two nanoscale iron particles, Environ. Sci. Technol. 39 (2004) 1338–1345.
[19] J.S. Cao, D. Elliott, W.X. Zhang, Perchlorate reduction by nanoscale iron particles, J. Nanoparticle Res. 7 (2005) 499–506, https://doi.org/10.1007/s11051-005-4412-x.
[20] A. Bampaiti, F. Noli, P. Misaelides, Investigation of the Cr(VI) removal from aqueous solutions by stabilized iron-nanoparticles using ^{51}Cr-tracer, J. Radioanal. Nucl. Chem. 298 (2013) 909–914, https://doi.org/10.1007/s10967-013-2483-1.
[21] C. Jing, Y.L. Li, S. Landsberger, Review of soluble uranium removal by nanoscale zero valent iron, J. Environ. Radioact. 164 (2016) 65–72, https://doi.org/10.1016/j.jenvrad.2016.06.027.
[22] L. Ling, W.X. Zhang, Enrichment and encapsulation of uranium with iron nanoparticle, J. Am. Chem. Soc. 137 (2015) 2788–2791, https://doi.org/10.1021/ja510488r.
[23] X.Q. Wu, Q. Yang, D.C. Xu, Y. Zhong, K. Luo, X.M. Li, H.B. Chen, G.M. Zeng, Simultaneous adsorption/reduction of bromate by nanoscale zerovalent iron supported on modified activated carbon, Ind. Eng. Chem. Res. 52 (2013) 12574–12581, https://doi.org/10.1021/ie4009524.
[24] J. Xu, T.T. Sheng, Y.J. Hu, S.A. Baig, X.S. Lv, X.H. Xu, Adsorption–dechlorination of 2,4-dichlorophenol using two specified MWCNTs-stabilized Pd/Fe nanocomposites, Chem. Eng. J. 219 (2013) 162–173, https://doi.org/10.1016/j.cej.2013.01.010.
[25] J. Xu, Z. Cao, Y. Wang, Y.L. Zhang, X.Y. Gao, M.B. Ahmed, J. Zhang, Y. Yang, J. L. Zhou, G.V. Lowry, Distributing sulfidized nanoscale zerovalent iron onto phosphorus-functionalized biochar for enhanced removal of antibiotic florfenicol, Chem. Eng. J. 359 (2019) 713–722, https://doi.org/10.1016/j.cej.2018.11.180.
[26] J. Xu, A. Avellan, H. Li, X.T. Liu, V. Noël, Z.M. Lou, Y. Wang, R. Kaegi, G. Henkelman, G.V. Lowry, Sulfur loading and speciation control the hydrophobicity, electron transfer, reactivity, and selectivity of sulfidized nanoscale zerovalent iron, Adv. Mater. 32 (2020) 1906910, https://doi.org/10.1002/adma.201906910.
[27] J. Xu, Z. Cao, H. Zhou, Z. Lou, Y. Wang, X.H. Xu, G.V. Lowry, Sulfur dose and sulfidation time affect reactivity and selectivity of post-sulfidized nanoscale zerovalent iron, Environ. Sci. Technol. 53 (2019) 13344–13352, https://doi.org/10.1021/acs.est.9b04210.
[28] J. Xu, Y. Wang, C. Weng, W.L. Bai, Y. Jiao, R. Kaegi, G.V. Lowry, Reactivity, selectivity, and long-term performance of sulfidized nanoscale zerovalent iron with different properties, Environ. Sci. Technol. 53 (2019) 5936–5945, https://doi.org/10.1021/acs.est.9b00511.
[29] Z. Cao, X. Liu, J. Xu, J. Zhang, Y. Yang, J.L. Zhou, X.H. Xu, G.V. Lowry, Removal of antibiotic florfenicol by sulfide-modi#ed nanoscale zero-valent iron, Environ. Sci. Technol. 51 (2017) 11269–11277, https://doi.org/10.1021/acs.est.7b02480.
[30] S. Luo, T.T. Lu, L. Peng, J.H. Shao, Q.R. Zeng, J.D. Gu, Synthesis of nanoscale zero-valent iron immobilized in alginate microcapsules for removal of Pb(II) from aqueous solution, J. Mater. Chem. A. 2 (2014) 15463–15472, https://doi.org/10.1039/c4ta02920h.
[31] J.J. Zhan, T.H. Zheng, G. Piringer, C. Day, G.L. Mcpherson, Y. Lu, K. Papadopoulos, V.T. John, Transport characteristics of nanoscale functional zerovalent iron/silica composites for in situ remediation of trichloroethylene, Environ. Sci. Technol. 42 (2008) 8871–8876, https://doi.org/10.1021/es800387p.
[32] Y.B. Hu, X.Y. Li, Influence of a thin aluminum hydroxide coating layer on the suspension stability and reductive reactivity of nanoscale zero-valent iron, Appl. Catal. B Environ. 226 (2018) 554–564, https://doi.org/10.1016/j.apcatb.2017.12.077.
[33] Y. Hwang, Y.C. Lee, P.D. Mines, Y.K. Oh, J.S. Choi, H.R. Andersen, Investigation of washing and storage strategy on aging of Mg-aminoclay (MgAC) coated nanoscale zero-valent iron (nZVI) particles, Chem. Eng. Sci. 119 (2014) 310–317, https://doi.org/10.1016/j.ces.2014.08.002.
[34] A.A. Pilarska, Ł. Klapiszewski, T. Jesionowski, Recent development in the synthesis, modification and application of $Mg(OH)_2$ and MgO: A review, Powder Technol. 319 (2017) 373–407, https://doi.org/10.1016/j.powtec.2017.07.009.
[35] Y.B. Hu, M.Y. Zhang, R.L. Qiu, X.Y. Li, Encapsulating nanoscale zero-valent iron with a soluble $Mg(OH)_2$ shell for improved mobility and controlled reactivity release, J. Mater. Chem. A. 6 (2018) 2517–2526, https://doi.org/10.1039/c7ta08605a.
[36] M.H. Liu, Y.H. Wang, L.T. Chen, Y. Zhang, Z. Lin, $Mg(OH)_2$ supported nanoscale zero valent iron enhancing the removal of Pb(II) from aqueous solution, ACS Appl. Mater. Interfaces. 7 (2015) 7961–7969, https://doi.org/10.1021/am509184e.
[37] [ISO 2597-1: 2016, Iron Ores-Determination of total iron content-Part 1: Titrimetric method after tin (II) chloride reduction, MOD].
[38] A. Gładysz-Płaska, E. Grabias, M. Majdan, Simultaneous adsorption of uranium(VI) and phosphate on red clay, Prog. Nucl. Energy. 104 (2018) 150–159, https://doi.org/10.1016/j.pnucene.2017.09.010.
[39] S. Chen, J. Bedia, H. Li, L.Y. Ren, F. Naluswata, C. Belver, Nanoscale zero-valent iron@mesoporous hydrated silica core-shell particles with enhanced dispersibility, transportability and degradation of chlorinated aliphatic hydrocarbons, Chem. Eng. J. 343 (2018) 619–628, https://doi.org/10.1016/j.cej.2018.03.011.
[40] D.L. Huang, Z.X. Hu, Z.W. Peng, G.M. Zeng, G.M. Chen, C. Zhang, M. Cheng, J. Wan, X. Wang, X. Qin, Cadmium immobilization in river sediment using stabilized nanoscale zero-valent iron with enhanced transport by polysaccharide coating, J. Environ. Manage. 210 (2018) 191–200, https://doi.org/10.1016/j.jenvman.2018.01.001.
[41] X. Zhang, S. Lin, Z.L. Chen, M. Megharaj, R. Naidu, Kaolinite-supported nanoscale zero-valent iron for removal of Pb^{2+} from aqueous solution: Reactivity, characterization and mechanism, Water Res. 45 (2011) 3481–3488, https://doi.org/10.1016/j.watres.2011.04.010.
[42] Y.D. Zou, X.X. Wang, A. Khan, P.Y. Wang, Y.H. Liu, A. Alsaedi, T. Hayat, X. K. Wang, Environmental remediation and application of nanoscale zero-valent iron and its composites for the removal of heavy metal ions: A review, Environ. Sci. Technol. 50 (2016) 7290–7304, https://doi.org/10.1021/acs.est.6b01897.
[43] G.D. Sheng, J. Hu, H. Li, J.X. Li, Y.Y. Huang, Enhanced sequestration of Cr(VI) by nanoscale zero-valent iron supported on layered double hydroxide by batch and XAFS study, Chemosphere 148 (2016) 227–232, https://doi.org/10.1016/j.chemosphere.2016.01.035.
[44] S.J. Yu, X.X. Wang, Y.F. Liu, Z.S. Chen, Y.H. Wu, Y. Liu, H.W. Pang, G. Song, J. R. Chen, X.K. Wang, Efficient removal of uranium(VI) by layered double hydroxides supported nanoscale zero-valent iron: A combined experimental and spectroscopic studies, Chem. Eng. J. 365 (2019) 51–59, https://doi.org/10.1016/j.cej.2019.02.024.
[45] B. Wu, D.H. Peng, S.Y. Hou, B.C. Tang, C. Wang, H. Xu, Dynamic study of Cr(VI) removal performance and mechanism from water using multilayer material coated nanoscale zerovalent iron, Environ. Pollut. 240 (2018) 717–724, https://doi.org/10.1016/j.envpol.2018.04.099.
[46] D.Q. Liu, Z.R. Liu, C.F. Wang, Y. Lai, Removal of uranium(VI) from aqueous solution using nanoscale zero-valent iron supported on activated charcoal, J. Radioanal. Nucl. Chem. 310 (2016) 1131–1137, https://doi.org/10.1007/s10967-016-4892-4.
[47] X.W. Zhang, L.J. Zhang, Y. Liu, M. Li, X.Y. Wu, T.J. Jiang, C. Chen, Y. Peng, Mn-substituted goethite for uranium immobilization: A study of adsorption behavior and mechanisms, Environ. Pollut. 262 (2020), 114184, https://doi.org/10.1016/j.envpol.2020.114184.
[48] T.Y. Liu, L. Zhao, D.S. Sun, X. Tan, Entrapment of nanoscale zero-valent iron in chitosan beads for hexavalent chromium removal from wastewater, J. Hazard. Mater. 184 (2010) 724–730, https://doi.org/10.1016/j.jhazmat.2010.08.099.
[49] R. Wang, G.H. Jing, X.B. Zhou, B.H. Lv, Removal of chromium(VI) from wastewater by Mg-aminoclay coated nanoscale zero-valent iron, J. Water Process Eng. 18 (2017) 134–143, https://doi.org/10.1016/j.jwpe.2017.05.013.
[50] G.C. Allen, N.R. Holmes, Surface characterisation of α-, β-, γ-, and δ-UO_3 using X-ray photoelectron spectroscopy, J. Chem. Soc. Dalt. Trans. 12 (1987) 3009–3015.
[51] J.J. Pireaux, N. Mårtensson, R. Didriksson, K. Siegbahn, J. Riga, J. Verbist, High resolution esca study of uranium fluorides: UF_4 and K_2UF_6, Chem. Phys. Lett. 46 (1977) 215–219, https://doi.org/10.1016/0009-2614(77)85246-9.
[52] O. Riba, T.B. Scott, K.V. Ragnarsdottir, G.C. Allen, Reaction mechanism of uranyl in the presence of zero-valent iron nanoparticles, Geochim. Cosmochim. Acta. 72 (2008) 4047–4057, https://doi.org/10.1016/j.gca.2008.04.041.
[53] X.Q. Li, W.X. Zhang, Sequestration of metal cations with zerovalent iron nanoparticles-A study with high resolution x-ray photoelectron spectroscopy (HR-XPS), J. Phys. Chem. C. 111 (2007) 6939–6946, https://doi.org/10.1021/jp0702189.
[54] B.J. Tan, K.J. Klabunde, P.M.A. Sherwood, XPS studies of solvated metal atom dispersed catalysts. Evidence for layered cobalt—manganese particles on alumina and silica, J. Am. Chem. Soc. 113 (1991) 855–861, https://doi.org/10.1021/ja00003a019.